Fermi energy dependence of first- and second-order Raman spectra in graphene: Kohn anomaly and quantum interference effect

Eddwi H. Hasdeo, Ahmad R. T. Nugraha, Mildred S. Dresselhaus, and Riichiro Saito

Phys. Rev. B **94**, 075104 — Published 2 August 2016

DOI: 10.1103/PhysRevB.94.075104

Fermi energy dependence of first- and second-order Raman spectra in graphene: Kohn anomaly and quantum interference effects

Eddwi H. Hasdeo[1],* Ahmad R. T. Nugraha[1], Mildred S. Dresselhaus[2,3], and Riichiro Saito[1]
[1]*Department of Physics, Tohoku University, Sendai 980-8578, Japan*
[2]*Department of Electrical Engineering, Massachusetts Institute of Technology, Cambridge, MA 02139-4307, USA*
[3]*Department of Physics, Massachusetts Institute of Technology, Cambridge, MA 02139-4307, USA*
(Dated: July 18, 2016)

Intensities of the first- and the second-order Raman spectra are calculated as a function of the Fermi energy. We show that the Kohn anomaly effect, i.e., phonon frequency renormalization, in the first-order Raman spectra originates from the phonon renormalization by the interband electron-hole excitation, whereas in the second-order Raman spectra, a competition between the interband and intraband electron-hole excitations takes place. By this calculation, we confirm the presence of different dispersive behaviors of the Raman peak frequency as a function of the Fermi energy for the first- and the second-order Raman spectra, as observed in some previous experiments. Moreover, the calculated results of the Raman intensity sensitively depend on the Fermi energy for both the first- and the second-order Raman spectra, indicating the presence of the quantum interference effect. The electron-phonon matrix element plays an important role in the intensity increase (decrease) of the combination (overtone) phonon modes as a function of the Fermi energy.

PACS numbers: 78.67.Ch, 73.22.-f, 42.65.Dr, 03.65.Nk

I. INTRODUCTION

Applying an electric gate voltage to graphene provides exotic tuning of the electronic, vibrational, and optical properties of graphene samples[1–3]. Since the beginning of graphene's discovery, electronic gating has played an important role in elucidating the room temperature quantum Hall effect[4–6], the Klein tunneling[7–9], and many body coupling effects[10,11]. Similar gating techniques are extensively applied not only to monolayer, but also to multilayer graphene to obtain tunable transport[12], a tunable band gap[13,14], p-n junctions[15], and photodetectors[16]. All of these exciting phenomena could be observed due to the ability to tune graphene's Fermi energy $E_{\rm F}$ through the applied gate voltage.

A combination of electronic gating and inelastic scattering of light, known as the gate modulated Raman spectroscopy[17], opens up a new possibility to understand more thoroughly the interplay of the electron, photon and phonon excitations in graphene. Several phenomena have been probed by gate modulated Raman spectroscopy in graphene, such as the Kohn anomaly (KA) effect or the phonon frequency renormalization[18–22], the quantum interference effect[23,24], electron-electron interaction[25], and the Fano resonance in the Raman spectra of graphene[26,27]. Studying gate modulated Raman spectroscopy in graphene has also enriched our knowledge of phonon spectra characterization[28], experimental evaluation of electron-phonon coupling[29], and various edge characterization effects[30,31].

Some theoretical works have been previously performed to understand the Kohn anomaly (KA) effect for the first-order Raman (G band) spectra with a Raman shift of $\sim$1600 cm^{-1} in graphene, such as those by Ando and the Mauri's groups[19,20,32]. In the KA process, phonon renormalization occurs through the excitation of an electron-hole pair by the electron-phonon interaction. As a result, the phonon energy is modified and the phonon lifetime becomes shorter. The previous theories mention that the phonon frequency shows a logarithmic singularity at $T = 0$ K when the absolute value of the Fermi energy $E_{\rm F}$ matches half of the phonon energy $|E_{\rm F}| = \hbar\omega_{\rm G}/2$. For $|E_{\rm F}| > \hbar\omega_{\rm G}/2$, the frequency shift is linearly proportional to $|E_{\rm F}|$. These predictions were already confirmed by Raman measurements[17,21,22,29,33]. Recently, additional experimental results allow us to study the KA effect in the second-order Raman spectra, also.

In contrast to the first-order Raman spectra that consist of only a single $\mathbf{q} = 0$ value of the phonon momentum, the second-order Raman spectra deals with the whole range of phonon momenta in the Brillouin zone satisfying the double resonance Raman condition[34]. Raman spectral features such as the G′ or 2D band ($\sim$ 2600 cm^{-1}) and the G* or D+D″ band ($\sim$ 2400 cm^{-1}) are observed as the second-order Raman spectra for $\mathbf{q} \approx$ K. The nonzero momentum phonon leads to a different KA effect compared with that for the $\mathbf{q} = 0$ phonon. Araujo *et al.* and Mafra *et al.* have shown that the frequency shift of the G′ band as a function of $E_{\rm F}$ is monotonically decreasing as a function of $|E_{\rm F}|$ which is opposite to that of the G band[22,28]. The other band at $\sim$ 2470 cm^{-1} is, however, dispersionless as a function of $E_{\rm F}$. Yan *et al.* show opposite results, that the G′ band frequency as a function of $E_{\rm F}$ has the same trends as that of the G band[29]. Further, Das *et al.* show an asymmetric G′ band dispersion, i.e., a positive (negative) slope of frequency shift at negative (positive) $E_{\rm F}$, which is inconsistent with a symmetric dispersion shown experimentally by Araujo *et al.* [21,22]. Based on the controversies in experimental results, we present calculated results of the second-order Raman spectra as a function of $E_{\rm F}$ from which we understand

the origin of the controversial results.

Sasaki et al, attempted to understand why the frequency shift of the G′ band KA has an opposite slope when compared with that of the G band from the viewpoint of the competition of interband and intraband electron-hole excitation in phonon perturbation[35]. However, since the theory is done within the effective mass approximation, it is not sufficient to explain the asymmetry of the G′ band frequency shift at positive and negative $E_{\rm F}$. Moreover, since the Raman intensity as a function of $E_{\rm F}$ is not calculated, different dispersion of Raman peaks as a function of $E_{\rm F}$ cannot be explained by that theory.

Observing the change of Raman intensity as a function of $E_{\rm F}$ reveals the quantum interference effect. When $E_{\rm F} \neq 0$, some Raman scattering paths are suppressed due to the Pauli exclusion principle. Even with the reduced number of scattering paths, the Raman intensity surprisingly increases at a particular value of $E_{\rm F}$ when destructive Raman phases among various scattering paths are suppressed. Chen *et al.* show that the G band Raman intensity gives a maximum value when $2|E_{\rm F}| = E_{\rm L} - \hbar\omega_G/2$, where $E_{\rm L}$ is the laser energy[23]. However, the theoretical analysis in their work assumes a constant matrix element, therefore neglecting the change of the Raman phase due to the electron-phonon matrix elements. Previous theoretical calculations show that the electron-phonon matrix elements change sign along electronic equi-energy lines in graphene and therefore can change the Raman phase[36,37]. A comprehensive calculation is, therefore, necessary to understand how the quantum interference effect affects the first- and the second-order Raman intensity.

In this work, we calculate the $E_{\rm F}$ dependence of the first-order and the second-order Raman spectra. The calculated spectral quantities are the Raman peak shift, spectral linewidth, and the Raman intensity as a function of $E_{\rm F}$. The KA correction including both the phonon frequency shift and the linewidth is modeled based on second-order perturbation theory. The KA of the first-order Raman spectra or of the $\mathbf{q} = 0$ phonon is calculated so as to reproduce the existing theoretical and experimental results and to compare with the KA of the $\mathbf{q} \neq 0$ phonon.We now focus on the intervalley scatterings which give three prominent peaks in the experimental spectra, namely, the G′, the G*, and the iTA + iTO bands, and are relevant to $\mathbf{q} \approx$ K. The $E_{\rm L}$ dependence of those Raman peak positions is compared with experimental results in order to justify the present calculation methods. Finally, the $E_{\rm F}$ dependences of those three Raman spectra are analyzed and compared to the experimental results.

The organization of this paper is as follows. Section II A shows the method for calculating the Raman intensities for the first- and second-order Raman spectra. Section II B explains the method for numerically calculating the KA effect. Section III A presents the calculated results of the KA effect for the $\mathbf{q} = 0$ phonon and the $E_{\rm F}$ dependence of the G band intensity. Section III B presents the calculation results of the KA effect for $\mathbf{q} \neq 0$, and the $E_{\rm L}$ and $E_{\rm F}$ dependence of the second-order Raman spectra. Finally, the conclusion is given in Sect. IV.

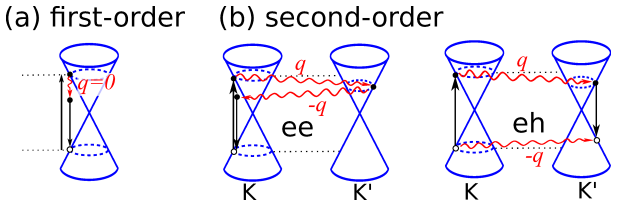

FIG. 1. (Color online) Schematics of (a) the first- and (b) the second-order Raman process. In (b), ee means two consecutive electron-phonon interactions while eh means electron-phonon interaction followed by hole-phonon interaction.

II. CALCULATION METHODS

A. Raman Intensity

The first-order Raman process as shown in Fig.1(a) consists of (1) excitation of an electron-hole pair by the electron-photon interaction, (2) phonon emission by means of the electron-phonon interaction, and (3) electron-hole recombination and photoemission by the electron-photon interaction. Based on the three subprocesses, the Raman intensity formula for the first-order Raman process is given by

$$I^{(1)} = \sum_{\nu} \left| \sum_{\mathbf{k}} \frac{M_{\rm op}^{\rm vc}(\mathbf{k}) M_{\rm ep}^{{\rm eh}\nu}(\mathbf{k},\mathbf{k}) M_{\rm op}^{\rm cv}(\mathbf{k}) \left[f(E_{\mathbf{k}}^{\rm v}) - f(E_{\mathbf{k}}^{\rm c}) \right]}{(E_{\rm L} - E_{\mathbf{k}}^{\rm cv} - i\gamma)(E_{\rm L} - E_{\mathbf{k}}^{\rm cv} - \omega_0^{\nu} - i\gamma)} \right|^2 \times \delta(E_{\rm L} - \omega_0^{\nu} - E_{\rm s}), \quad (1)$$

where $E_{\rm L}$ is the laser excitation energy, $E_{\rm s}$ is the scattered photon energy, $E_{\mathbf{k}}^{\rm cv} = E_{\mathbf{k}}^{\rm c} - E_{\mathbf{k}}^{\rm v}$ is the electron energy difference between the conduction (c) and the valence (v) bands at a wave vector $\mathbf{k}$, $\gamma = (37.6E_{\rm L} + 13.6E_{\rm L}^2) \times 10^{-3}$ eV is the carrier scattering rate due to the electron-phonon interaction[38], and $f(E)$ is the Fermi distribution function which depends on temperature. $M_{\rm op}^{\rm cv}(\mathbf{k})$ is the electron-photon matrix element accounting for the optical transition of an electron in a state $\mathbf{k}$ from a valence band to a conduction band, $M_{\rm ep}^{{\rm eh}\nu}(\mathbf{q},\mathbf{p}) = M_{\rm ep}^{{\rm cc}\nu}(\mathbf{q},\mathbf{p}) - M_{\rm ep}^{{\rm vv}\nu}(\mathbf{q},\mathbf{p})$ is the carrier-phonon interaction considering an electron (e) in a conduction band or a hole (h) in a valence band making a transition from a state $\mathbf{p}$ to a state $\mathbf{q}$ by emitting a phonon with momentum $\mathbf{q} - \mathbf{p}$, mode ν, and frequency $\omega_{\mathbf{q}-\mathbf{p}}^{\nu}$. Hereafter, $\hbar = 1$ is used, so that $\omega_{\mathbf{q}-\mathbf{p}}^{\nu}$ has units of energy. For the case of a one phonon process, only zero momentum or the Γ point phonon is relevant. The summation over $\mathbf{k}$ in Eq. (1) is taken to occur in a uniform square mesh, with a mesh spacing $\Delta k = \gamma/2v$, and $v = 6.46$ eVÅ is the slope of the electron energy dispersion of graphene and Δk^2 is the weight of the integration.

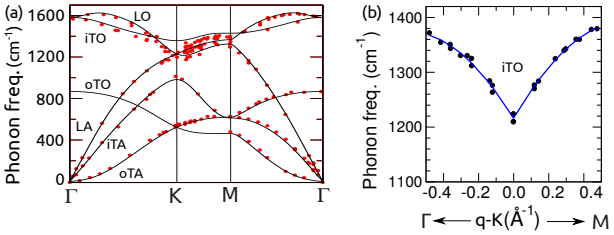

FIG. 2. (Color online) (a) Calculated (solid lines, this work) and experimental (red dots, from Refs. 45 and 46) phonon dispersion relations. (b) Fitting of Eq. (2) (blue line) to the iTO branch from Ref. 47 (dots) near the K point.

We set a cutoff energy $E_{\rm cut} = 3.5$ eV for $E^{\rm cv}_{\mathbf{k}}$ so as to reduce the number of mesh points in the Brillouin zone integration. It is important to note that both the numerator and denominator of Eq. (1) are complex numbers, thus the summation of $\mathbf{k}$ before taking the square plays an important role in the quantum interference effect[39,40].

The electronic structure of graphene is calculated within an extended tight binding method considering up to 20 nearest neighbors and the four atomic orbitals ($2p_x$, $2p_y$, $2p_z$, $2s$)[41,42]. Calculation of the phonon dispersion relations is performed within a force constant model with the interatomic potential including up to 20 nearest neighbors which is fitted from a first-principles calculation[43,44]. Figure 2(a) shows the calculated results of the phonon dispersion relations (solid lines) and the corresponding experimental phonon dispersion relations (red dots) for comparison from Refs. 45 and 46. Because of the KA effect, the dispersion of the in-plane tangential optic (iTO) branch near the K point is discontinuous along the $\Gamma-{\rm K}-{\rm M}$ path which cannot be reproduced by the force constant model[19]. We fit the iTO frequency from the experiment[47] and use the following fitting formula for the Raman spectra calculation [Fig. 2(b)]:

$$\omega^{\rm iTO}_{\mathbf{q}} = \big\{ -424.81q^2 + 534.47q + 1215.95 + (6.94q^2 + 10.89q)\cos(3\theta) \big\}\ {\rm cm}^{-1}, \quad (2)$$

where $\mathbf{q}$ is defined using polar coordinates (q,θ) whose center is at the K point and θ is measured from the KM direction. Eq. (2) is valid only for $q \le 0.4$ Å^{-1}, and when $q > 0.4$ Å^{-1}, we use the results from the force constant model for $\omega^{\rm iTO}_{\mathbf{q}}$.

In the electron-photon interaction, we adopt a dipole approximation, i.e., assuming a slowly varying electric field in space because the laser wavelength is much greater than the inter-atomic distance[48]. The electron-phonon interaction is calculated using the tight binding method with the deformation potential fitted from the GW method for the K and Γ points[38].

In the second-order Raman processes, phonons with modes ν and μ and momenta $\mathbf{q}$ and $-\mathbf{q}$, respectively, are emitted [Fig. 1(b)]. Depending on the carriers taking part in the scattering event, the Raman intensity formula is given by:

$$I^{(2)} = \sum_{\mathbf{q}\nu\mu} \big| A^{\rm ee}_{\mathbf{q}\nu\mu} + A^{\rm hh}_{\mathbf{q}\nu\mu} + A^{\rm he}_{\mathbf{q}\nu\mu} + A^{\rm eh}_{\mathbf{q}\nu\mu} + A^{\rm ee}_{-\mathbf{q}\mu\nu} + A^{\rm hh}_{-\mathbf{q}\mu\nu} + A^{\rm he}_{-\mathbf{q}\mu\nu} + A^{\rm eh}_{-\mathbf{q}\mu\nu} \big|^2 \times \delta(E_{\rm L} - \omega_\nu - \omega_\mu - E_{\rm s}), \quad (3)$$

where $A^{\rm eh}_{\mathbf{q}\nu\mu}$ is a Raman amplitude for each process: (1) an electron (e), first, emits a ν phonon with momentum $\mathbf{q}$ and, (2) a hole (h) emits the μ phonon with momentum $-\mathbf{q}$. Here, $A^{\rm eh}_{\mathbf{q}\nu\mu}$ and $A^{\rm eh}_{-\mathbf{q}\mu\nu}$ are not equivalent to each other due to the different time order of the two phonon emission. Next, we show examples of the Raman amplitude formula for $A^{\rm ee}_{\mathbf{q}\nu\mu}$ and $A^{\rm eh}_{\mathbf{q}\nu\mu}$:

$$A^{\rm ee}_{\mathbf{q}\nu\mu} = \sum_k \frac{M^{\rm vc}_{\rm op}(\mathbf{k}) M^{{\rm cc}\mu}_{\rm ep}(\mathbf{k},\mathbf{k}+\mathbf{q}) M^{{\rm cc}\nu}_{\rm ep}(\mathbf{k}+\mathbf{q},\mathbf{k}) M^{\rm cv}_{\rm op}(\mathbf{k}) \left[f(E^{\rm v}_{\mathbf{k}}) - f(E^{\rm c}_{\mathbf{k}}) \right]}{(E_{\rm L} - E^{\rm cv}_{\mathbf{k}} - i\gamma)(E_{\rm L} - E^{\rm c}_{\mathbf{k}+\mathbf{q}} + E^{\rm v}_{\mathbf{k}} - \omega^\nu_{-\mathbf{q}} - i\gamma)(E_{\rm L} - E^{\rm cv}_{\mathbf{k}} - \omega^\nu_{-\mathbf{q}} - \omega^\mu_{\mathbf{q}} - i\gamma)}, \quad (4)$$

$$A^{\rm eh}_{\mathbf{q}\nu\mu} = -\sum_k \frac{M^{\rm vc}_{\rm op}(\mathbf{k}+\mathbf{q}) M^{{\rm vv}\mu}_{\rm ep}(\mathbf{k}+\mathbf{q},\mathbf{k}) M^{{\rm cc}\nu}_{\rm ep}(\mathbf{k}+\mathbf{q},\mathbf{k}) M^{\rm cv}_{\rm op}(\mathbf{k}) \left[f(E^{\rm v}_{\mathbf{k}}) - f(E^{\rm c}_{\mathbf{k}}) \right]}{(E_{\rm L} - E^{\rm cv}_{\mathbf{k}} - i\gamma)(E_{\rm L} - E^{\rm c}_{\mathbf{k}+\mathbf{q}} + E^{\rm v}_{\mathbf{k}} - \omega^\nu_{-\mathbf{q}} - i\gamma)(E_{\rm L} - E^{\rm cv}_{\mathbf{k}+\mathbf{q}} - \omega^\nu_{-\mathbf{q}} - \omega^\mu_{\mathbf{q}} - i\gamma)}. \quad (5)$$

The minus sign in Eq. (5) corresponds to the opposite charge of the hole from the electron in the hole-phonon matrix elements[49].

B. The Kohn Anomaly

Kohn mentions that conduction electrons are able to screen phonons in a metal[18]. This screening leads to a phonon frequency change, given by:

$$\omega^\nu_{\mathbf{q}} = \omega^{(0),\nu}_{\mathbf{q}} + \omega^{(2),\nu}_{\mathbf{q}}, \quad (6)$$

where $\omega^{(0),\nu}_{\mathbf{q}}$ is the unperturbed phonon energy from the phonon dispersion relation. Here, $\omega^{(2),\nu}_{\mathbf{q}}$ is the correction term taken from the second-order perturbation of the electron-phonon interaction by the excitation and re-

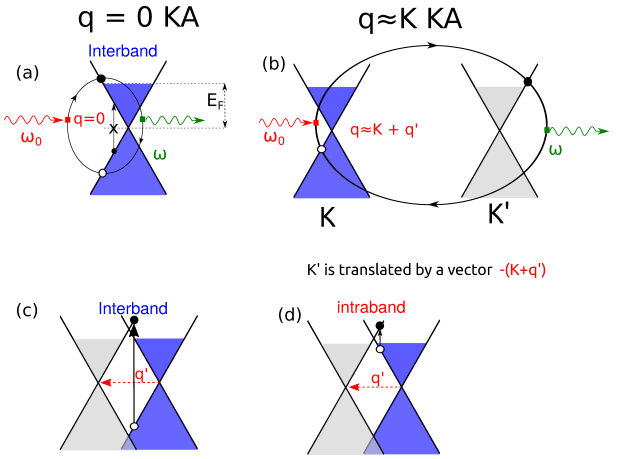

FIG. 3. (Color online) (a) A schematic of the $\mathbf{q} = 0$ Kohn anomaly process. A phonon with zero wave vector ($\mathbf{q} = 0$) and frequency ω_0 vertically excites an electron-hole pair via the electron-phonon interaction. The electron-hole pair then recombines by emitting a phonon with frequency ω. (b) A schematic of the $\mathbf{q} \approx$ K Kohn anomaly process. An electron exists at the K′ point leaving a hole behind at the K point with a distance in reciprocal space of $\mathbf{q} = \mathrm{K} + \mathbf{q}'$. If the K′ point is then translated by a vector $-(\mathbf{K}+\mathbf{q}')$, we can then imagine a virtual vertical transition of electron and hole. When $E_\mathrm{F} \neq 0$, both interband (c) and intraband (d) transitions are expected.

combination of an electron-hole pair (Fig. 3):

$$\omega_{\mathbf{q}}^{(2),\nu} = 2\sum_{s,s'}^{\mathrm{c,v}}\sum_{\mathbf{k}} \frac{|M_{\mathrm{ep}}^{ss'\nu}(\mathbf{k},\mathbf{k}+\mathbf{q})|^2 \left[f(E_{\mathbf{k}}^{s}) - f(E_{\mathbf{k}+\mathbf{q}}^{s'})\right]}{\omega_{\mathbf{q}}^{(0),\nu} - E_{\mathbf{k}+\mathbf{q}}^{s'} + E_{\mathbf{k}}^{s} + i\eta}, \tag{7}$$

where the prefactor 2 in Eq. (7) accounts for the spin degeneracy, while the valley degeneracy is considered in the summation over $\mathbf{k}$. The value of $\omega_{\mathbf{q}}^{(2),\nu}$ is a complex number, in which $\mathrm{Re}(\omega_{\mathbf{q}}^{(2),\nu})$ [$-\mathrm{Im}(\omega_{\mathbf{q}}^{(2),\nu})$] gives the phonon frequency shift [phonon linewidth]. In Eq. (7), the contribution of the interband (intraband) electron-hole pair appears at $s \neq s'$ ($s = s'$).

In a conventional 2D electron gas, the KA effect occurs at $\mathbf{q} = 2\mathbf{k}_\mathrm{F}$, where $\mathbf{k}_\mathrm{F}$ is the Fermi wave vector. In graphene, due to its unique linear energy bands, the KA occurs at $\mathbf{q} \approx 0$ and $\mathbf{q} \approx$ K. The schematics of the KA process for $\mathbf{q} = 0$ and $\mathbf{q} \approx$ K are shown in Figs. 3(a) and (b), respectively. In the $\mathbf{q} = 0$ KA, a phonon with frequency ω_0 vertically excites an electron-hole pair via the electron-phonon interaction [Fig. 3(a)]. The electron-hole pair then recombines by emitting a phonon with frequency ω. In the $\mathbf{q} \approx$ K KA, an electron exists at the K′ point, leaving a hole behind at the K point with a distance in reciprocal space $\mathbf{q} = \mathrm{K} + \mathbf{q}'$ [Fig. 3(b)]. If the K′ point is translated by a vector $-(\mathbf{K}+\mathbf{q}')$, we can imagine a virtually vertical excitation of an electron-hole pair. When $E_\mathrm{F} \neq 0$, both the interband [Fig. 3(c)] and intraband [Fig. 3(d)] transitions are expected.

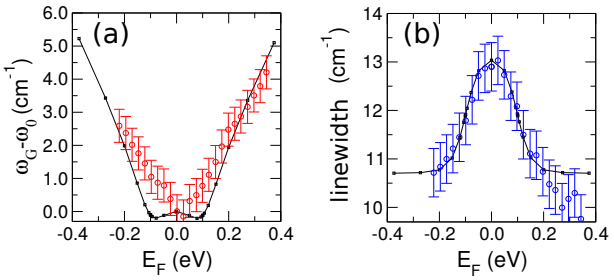

FIG. 4. (Color online) The calculated (dotted line) and experimental (open circles) results for the G band peak shift (a) and the G band linewidth (b) as a function of the Fermi energy, respectively, for $T = 300$ K.

III. RESULTS AND DISCUSSION

A. First-order Raman spectra

Employing Eq. (7) at $\mathbf{q} = 0$, we can obtain the frequency shift [Fig. 4(a)] and phonon linewidth [Fig. 4(b)] for the G band as a function of the Fermi energy at $T = 300$ K. In Fig. 4 we show the calculated (dotted line) and experimental (open circles) results[22] of the G band peak shift and linewidth as a function of the Fermi energy, respectively. The calculated results are in good agreement with the experimental results. In Fig. 4(a), we see dips when $2|E_\mathrm{F}| = \omega_0 \approx 0.2$ eV for the calculation, while the experimental results do not show such dips. These dips are originated from the logarithmic singularities at $T = 0$ K and are related to interband resonances[20,32,50]. For $2|E_\mathrm{F}| > \omega_0$, the G band frequency increases linearly as a function of the Fermi energy. At 0 K, the phonon linewidth shows a step function $\theta(\omega_0 - 2|E_\mathrm{F}|)$. The step function indicates that when $2|E_\mathrm{F}| > \omega_0$, the phonon linewidth from the KA effect becomes zero since no excited electron-hole pair meets the resonance condition of Eq. (7). At finite T, on the other hand, the Fermi distribution function becomes a smooth function and that is why we get a smooth function of the linewidth as a function of E_F. It is noted that we add an extrinsic broadening of 10.3 cm^{-1} in our calculations in order to fit with experimental results[22] in Fig. 4(b).

Next, we calculate the Raman spectra of the G band using Eq. (1). The G band consists of both the $\mathbf{q} = 0$ longitudinal optic (LO) and in-plane-tangential optic (iTO) modes. In order to understand their contributions to the Raman amplitudes at each $\mathbf{k}$ point, we plot the real and imaginary parts of the Raman amplitude in Eq. (1) for LO and iTO phonons in Fig. 5(a) and (b), respectively. Here we use $E_\mathrm{L} = 2.33$ eV and take $E_\mathrm{cut} = 3.5$ eV so as to reduce the total points of integration for saving computational time. It will be clear that neglecting the contributions from energies above E_cut in the integration is reasonable since the Raman intensity is quickly decreasing when $2|E_\mathrm{F}| > E_\mathrm{cut}$. In Fig. 5, deformed triangles near the K and the K′ points indicate equi-energy lines that

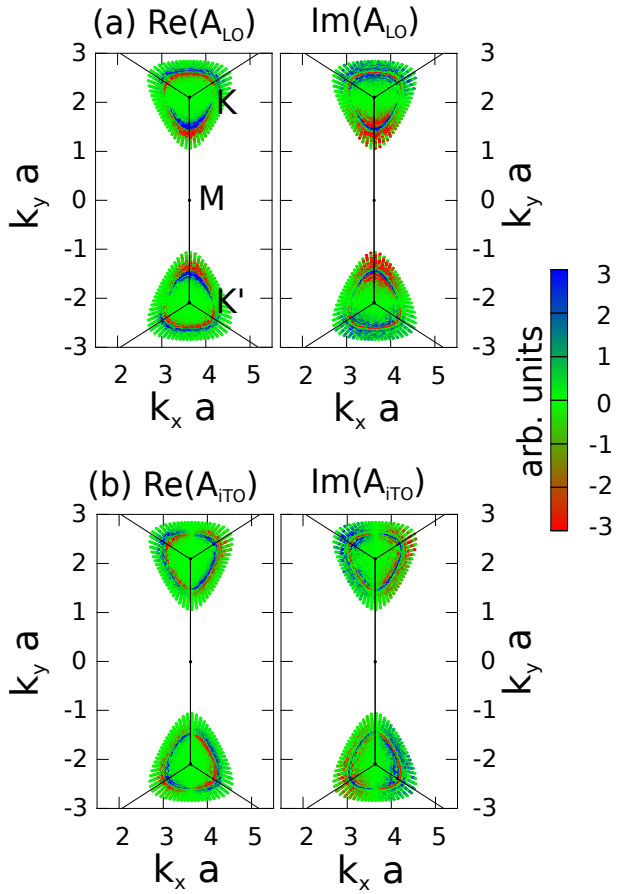

FIG. 5. (Color online) Calculated results of the real and imaginary parts of the first-order (a) LO and (b) iTO Raman amplitudes in a two dimensional Brillouin zone near the K and K′ points with $E_{\rm L} = 2.33$ eV.

match the resonant conditions. The lower (higher) resonant condition corresponds to the scattered (incident) resonance when $E_{\mathbf{k}}^{\rm cv} = E_{\rm L} - \omega_G$ ($E_{\mathbf{k}}^{\rm cv} = E_{\rm L}$) which is shown by a large amplitude at the inner (outer) line. We see changes in the sign for both the real and imaginary parts of the LO and iTO Raman amplitudes in both the radial and azimuthal directions. The change of sign at the radial direction is related to an opposite phase between the scattered resonance and the incident resonance. Meanwhile, the change of sign in the azimuthal direction is related to the sign of the electron-phonon matrix element as reported by Jiang et al[36]. The LO (iTO) phonon has a zero matrix element at the 0 ($\pi/2$) phase.

The opposite phases between the scattered resonance and the incident resonance are essential for calculating the Raman intensity as both terms give destructive interference. Therefore, only taking the resonant terms for calculating the Raman intensity is not sufficient to reproduce the experimental results. We need to at least consider up to $E_{\mathbf{k}}^{\rm cv} \approx E_{\rm L} + \omega_G$ to get a realistic intensity. Moreover, if we plot the Raman intensity as a function of the Fermi energy as shown in Fig. 6(a), it becomes clear that destructive interference between the scattered resonance and the incident resonance can be suppressed when we set the Fermi energy close to the laser excitation energy. When $2|E_{\rm F}| = E_{\rm L} - \omega_G/2$, the scattered resonance cannot occur due to the Pauli blocking effect [Fig. 6(b)]. Therefore, in Fig. 6(a) we see the largest G band intensity at $2|E_{\rm F}| = E_{\rm L} - \omega_G/2$ as pointed out by Chen *et al*[23]. The difference of the intensity at positive and negative $E_{\rm F}$ which comes from the electron-hole asymmetry has been confirmed by Liu *et al*[24]. Anisotropy in the azimuthal direction should give destructive interference, but the effect is negligible.

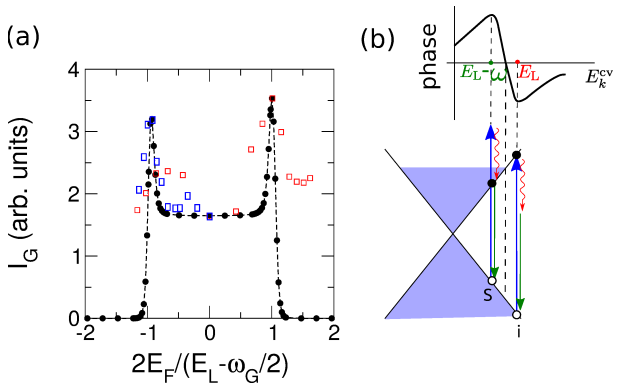

FIG. 6. (Color online) (a) Calculated results (black dots) and experimental results (blue squares from Ref. 23 and red squares from Ref. 24) of the G band Raman intensity as a function of the reduced Fermi energy. (b) Schematic diagram showing an opposite phase between the incident (i) and scattered (s) resonances. When $2|E_{\rm F}| = E_{\rm L} - \omega_G/2$, the scattered resonance is suppressed, and therefore, the Raman intensity gives a maximum value.

B. Second-order Raman spectra

In Fig. 7, we show the calculated results of the $\mathbf{q} \neq 0$ KA effect from Eq. (7). First, let us consider the case of $\mathbf{q} = $ K in Figs. 7(b) and (e). If we compare respectively Figs. 7(b) and (e) with Figs. 4(a) and (b), both the frequency shift and phonon linewidth show the same trends as that of $\mathbf{q} = 0$ KA because both $\mathbf{q} = 0$ and $\mathbf{q} = $ K are dominated by the interband electron-hole excitation. The reason why the interband excitation is dominant at $\mathbf{q} = $ K, is that the K and K′ points coincide upon translation of the K′ point by a vector $-$K [$\mathbf{q}' = 0$ in Fig. 3(c)]. Therefore, at the $\mathbf{q} = $ K KA, only virtually vertical interband excitation, the same as at $\mathbf{q} = 0$ KA, is possible[51]. The previous work did not consider the interband contribution, therefore assigning the $\mathbf{q} = $ K phonon frequency shift to be dispersionless as a function of $E_{\rm F}$[22].

Next, if we shift by $\xi = 0.14$ Å^{-1} from $\mathbf{q} = $ K, competition between the intraband and interband excitations take place as shown in Figs. 7(a), (c), (d), and (f). According to the analytical formula[51], the intraband contribution to the frequency shift is proportional

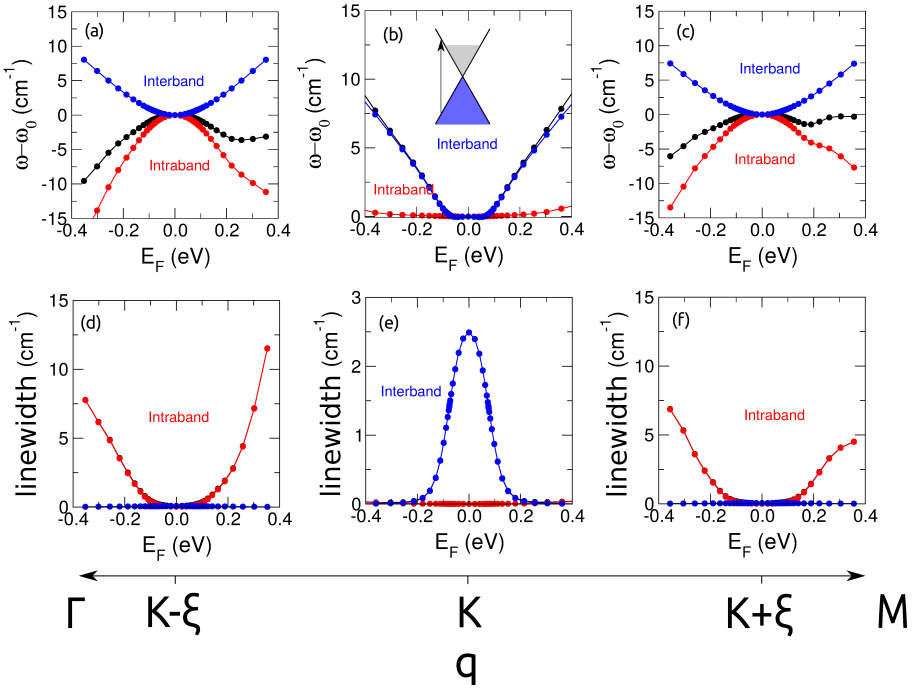

FIG. 7. (Color online) The iTO phonon energy shift and linewidth as a function of the Fermi energy $E_{\rm F}$ for (a), (d) $\mathbf{q} = \mathrm{K} - \xi$; (b), (e) $\mathbf{q} = \mathrm{K}$; and (c), (f) $\mathbf{q} = \mathrm{K} + \xi$, with $\xi = 0.14$ Å^{-1}. We use $T = 300$ K.

to $-\sin^{-1}|2E_{\rm F}/vq|$ by assuming $\omega_0 \ll vq$, where v is the slope of the linear energy dispersion of graphene which is ~ 6.46 eVÅ. The phonon linewidth is increasing linearly with $|E_{\rm F}|$ in the case of the intraband excitation [Figs. 7(d) and (f)] because the electron-phonon scattering rate is proportional to the carrier concentration. The asymmetry at positive and negative $E_{\rm F}$ is related to electron-hole band asymmetry considered in the tight binding calculation.

After considering the KA effect on the $\mathbf{q} \neq 0$ phonon, in Fig 8 we show the calculated Raman spectra from Eq. (3). Figure 8(a) shows three bands, respectively, assigned as the G′ ~ 2700 cm^{-1}, G* ~ 2500 cm^{-1}, and iTA + iTO ~ 2240 cm^{-1} for $E_{\rm L} = 1.53$ eV. We confirm the origin of the G′ bands from the overtone of the iTO (2iTO) modes while the G* bands come from a combination of iTO and LA modes. The major contributions to the G′ intensity come from the $A^{\rm eh}$ and $A^{\rm he}$ terms as shown by $ab = (A^{\rm eh} + A^{\rm he})$ in Fig. 8(b). This confirms the previous calculation that the $A^{\rm ee}$ and $A^{\rm hh}$ terms are negligible [$aa = (A^{\rm ee} + A^{\rm hh})$ in Fig. 8(b)] because of the quantum interference effect during the $\mathbf{k}$ integration[38].

Figure 8(c) shows the second-order Raman intensities for 1.53 eV $\leq E_{\rm L} \leq 2.41$ eV. The intensities of all these Raman bands are inversely proportional to $E_{\rm L}$ because of the increase of the electron-phonon scattering rate γ as a function of $E_{\rm L}$[38,55]. Assuming that each band can be represented by a single peak, the G′, G*, and iTA+iTO peak dispersions as a function of $E_{\rm L}$ are shown in Fig. 8(d). The G′ band shows a positive slope as a function of $E_{\rm F}$, i.e., 95 cm^{-1}/ eV in this work, 90 cm^{-1}/ eV in Ref. 52, and 104 cm^{-1}/ eV in Ref. 53. Meanwhile, the G* band shows a negative slope, i.e., -33 cm^{-1}/ eV in this work and -33 cm^{-1}/ eV in Ref. 52 and the iTA + iTO band slope is -58 cm^{-1}/ eV in this work, -56 cm^{-1}/ eV in Ref. 54, and -50 cm^{-1}/ eV in Ref. 28 [not shown in Fig. 8(d)]. Good agreement between theory and experiment in the slope of the $E_{\rm L}$ dispersion indicates the reliability of our phonon dispersion used in the calculation. However, discrepancies with the experiments of about 50 cm^{-1} in the G′ and the iTA + iTO bands for a given $E_{\rm L}$ show that the calculated electronic energy dispersion underestimates the experimental results. This can be seen insofar as the G′ and iTA + iTO peaks at $E_{\rm L} = 1.5$ eV in theory give relatively the same value for $E_{\rm L} = 2.0$ eV in the experiment, thus the present electronic energy dispersion near $E_{\rm L}$ underestimate the real value by ~ 0.5 eV. This might be because we neglect the many body effects in the band calculations. Nevertheless, the overall agreement is sufficient for us to proceed and consider the $E_{\rm F}$ dependence of the Raman intensity for a particular $E_{\rm L}$.

Figure 9 shows the evolution of the second-order Raman spectra for several values of $E_{\rm F}$. We use the same $E_{\rm L} = 2.33$ eV as Araujo *et al*[22]. In Figs. 9(a) and (b) the intensities have been multiplied by two times as indicated. Figures 9(a) and (d) show the decrease of the G′ peak intensity as $|E_{\rm F}|$ increases. In Fig. 9(d), the calculated results shown black circles and the experimental results (blue squares from Ref. 23 and red squares from Ref. 24) reasonably agree with each other. However, the Raman intensity of the iTA+iTO and G* bands dramati-

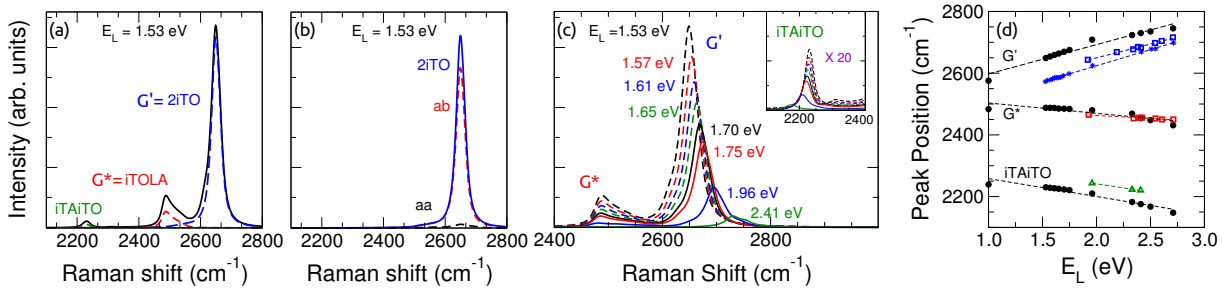

FIG. 8. (Color online) (a) The calculated results of the second-order Raman intensity for a laser energy 1.53 eV showing three significant peaks identified with the iTA+iTO band ($\sim$ 2200 cm^{-1}), iTO+LA or G* band ($\sim$ 2500 cm^{-1}), and 2iTO or 2D or G$'$ band ($\sim$ 2800 cm^{-1}). (b) The constituents of the G$'$ band contribution from (a): $ab = (A^{\rm eh} + A^{\rm he})$ (blue dashed line) and $aa = (A^{\rm ee} + A^{\rm hh})$ (red dashed line). (c) The calculated results of the $E_{\rm L}$ dependence of the G$'$, G*, and iTA + iTO bands (inset) for 1.53 eV $\leq E_{\rm L} \leq$ 2.41 eV. (d) The G$'$, G*, and iTA + iTO bands peak position as a function of $E_{\rm L}$. Black dots are the calculated results (this work), blue and red open squares are from Ref. 52, blue asterisks are from Ref. 53, and green triangles are from Ref. 54.

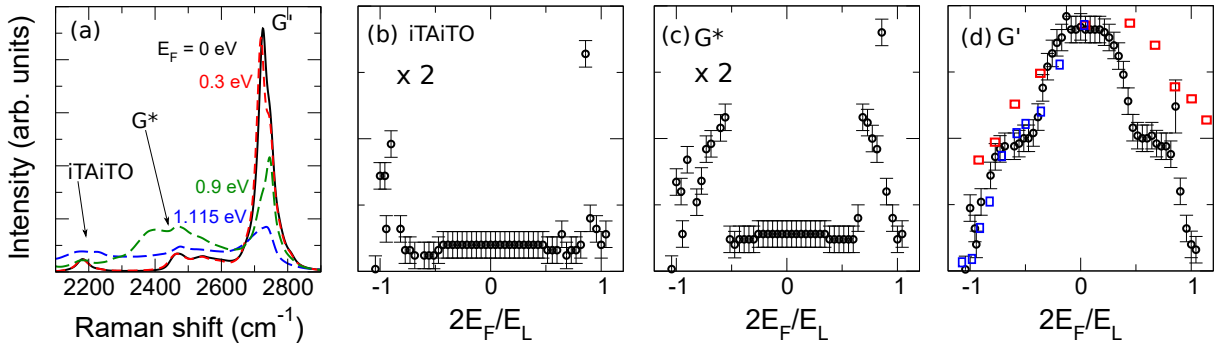

FIG. 9. (Color online) (a) The second-order Raman spectra for several $E_{\rm F}$. (b) iTA + iTO, (c) G*, and (d) G$'$ band intensities as a function of $2E_{\rm F}/E_{\rm L}$, where $E_{\rm L}$ = 2.33 eV. In panels (a) and (b) the intensities have been multiplied by two times as indicated in the figures. In panel (d), calculated results are represented by black circles, while experimental results are denoted by blue squares (from Ref. 23) and red squares (from Ref. 24).

cally increase at certain values of $E_{\rm F}$ as shown in Fig. 9(b) and (c), respectively. We find that the intensity increase of the combination phonon modes (iTA + iTO and G* bands) originates from the electron-phonon matrix elements effect to the phase of Raman spectra. Products of two electron-phonon matrix elements of the combination phonon modes (see Eq. (3)) give complex values with random phases as a function of $\mathbf{q}$ and $\mathbf{k}$. The random phases give destructive interference when integrating over $\mathbf{k}$ and $\mathbf{q}$ at $E_{\rm F} = 0$. At a finite $E_{\rm F}$, some of these destructive phases are suppressed due to the Pauli blocking, as a result, the Raman intensity for the combination phonon modes are enhanced. On the other hand, the overtone mode (G$'$) does not provide such a destructive phase because the two electron-phonon matrix elements are related by a complex conjugation and the product of the matrix elements gives only a real value. Therefore with the increase of $|E_{\rm F}|$, the G$'$ intensity decreases.

Figure 10(a) shows the Lorentzian fitting results on the second-order Raman spectra for $E_{\rm F} = 0$. The dotted line is the calculated Raman intensity fitted by six Lorentzians. We fit the G$'$ bands with two Lorentzians labeled by G$'_{\rm o}$ (blue) and G$'_{\rm i}$ (red) which refer to G$'$ bands from outer ($\mathbf{q}$ in KM direction) and inner ($\mathbf{q}$ in KΓ direction) scattering processes, respectively[38,53]. Three Lorentzians are needed to fit the G* band, labeled by G$^*_1$ (green), G$^*_2$ (blue), and G$^*_3$ (red). Finally, one Lorentzian is used to fit the iTA + iTO band.

After Lorentzian fitting, we compare both the peak shift and the spectral linewidth as a function of $E_{\rm F}$ as shown in Figs. 10(b)-(e). We do not show the G$'_{\rm o}$ and G$^*_1$ for simplicity because there is no experimental data available for comparison. The calculated results in Fig. 10(b)-(e) cannot fit the experimental value of both the peak position and the linewidth due to the underestimation of the electronic energy dispersion as previously discussed in the $E_{\rm L}$ dependence of the second-order Raman spectra [see Fig. 8(d)]. But we can discuss the change of both quantities as a function of $E_{\rm F}$, where the KA effect takes place. In Figs. 10(b)-(e), both the spectral peak position and the linewidth as a function of $E_{\rm F}$ are plotted in the same range, comparing the theory and experiments. Reasonable agreements between experiments and theory are achieved. The three major peaks, i.e., the G$'_{\rm i}$, G$^*_3$,

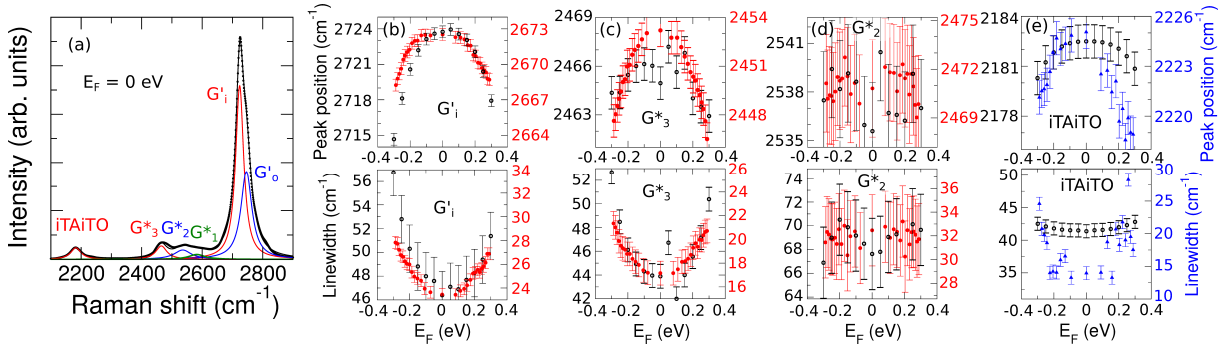

FIG. 10. (Color online) (a) Fitting of the second-order Raman spectra obtained in Fig. 9(a) at $E_{\rm F} = 0$ eV and $E_{\rm L} = 2.33$ eV. The dotted line is the calculated Raman intensity fitted by six Lorentzians labeled by $\rm G'_o$ (blue), $\rm G'_i$ (red), $\rm G^*_1$ (green), $\rm G^*_2$ (blue), $\rm G^*_3$ (red), and iTA + iTO bands. We show the peak shift and the spectral linewidth as a function of $E_{\rm F}$ for (b) the $\rm G'_i$, (c) $\rm G^*_3$, (d) $\rm G^*_2$, and (e) iTA + iTO bands. Black open circles are the results in this work, red closed circles are experimental results from Ref. 22, and blue triangles are experimental results from Ref. 28.

and iTA + iTO bands show "Λ" ("V") shapes of the Raman peak shift (spectral linewidth) as a function of $E_{\rm F}$. These behaviors exist because of the intraband electron-hole excitation renormalization of phonons as shown in Fig. 7. The $\rm G^*_2$ band in Fig. 10(d) is relatively dispersionless in $E_{\rm F}$ because it is located on the shoulder of the G′ band where 2iTO $\mathbf{q} = K$ exists. Therefore, for these bands, the competition between interband and intraband electron-hole excitations are expected. The calculated results overestimate the experimental spectral linewidth of all bands, which is related to the choice of $\Delta\mathbf{k}$ in the $\mathbf{k}$ integration. We can tackle this issue by reducing the value of $\Delta\mathbf{k}$ by $\Delta\mathbf{k}/n$; however, the computational burden becomes e^n times larger.

In order to clarify different experimental results from Ref. 21, Ref. 22, and Ref. 29, we show the G′ band peak position as a function of $E_{\rm F}$ in Fig. 11(a) with a range of -1.2 eV up to 1.2 eV, which is about the same range of measurement from Ref. 21. From Figs. 11(b) and 9(a), we show that at $E_{\rm F} = 0$, the G′ band intensity originating from the inner process ($\rm G'_i$) is larger than that from the outer process ($\rm G'_o$). However, at high doping ($|E_{\rm F}| \geq 0.5$ eV), the $\rm G'_i$ intensity becomes smaller than that of the ($\rm G'_o$) as $|E_{\rm F}|$ increases. The decrease of the $\rm G'_i$ band intensity has been pointed out in Fig. 9 as a result of the quantum interference effect. Because of the KA effect, the $\rm G'_i$ peak position is decreasing as $|E_{\rm F}|$ increases while the peak position of $\rm G'_o$ is shown to be constant (this origin should be presented elsewhere). The increased distance between $\rm G'_i$ and $\rm G'_o$ peak positions with the increase of $|E_{\rm F}|$ confirms the experimental results by Ref. 53. At $|E_{\rm F}| \geq 0.5$ eV, the $\rm G'_o$ feature cannot be fitted with a single Lorentzian, thus we add an additional Lorentzian $\rm G'_m$ to better fit with the total calculated spectra.

We compare the calculated results with the experimental results in Fig. 11(c). Since the G′ band peak position is $E_{\rm L}$ dependent and those three experiments use different $E_{\rm L}$ values (2.41 eV for Ref. 21, 2.54 eV for Ref. 29, and 2.33 eV for Ref. 22 and this calculation), we compare the G′ band peak position as a function of $2E_{\rm F}/E_{\rm L}$ relative to the peak position at $E_{\rm F} = 0$ (ω_0). The scaling of $2E_{\rm F}/E_{\rm L}$ is considered because when $2E_{\rm F} = E_{\rm L}$, we expect the interference effect to be significant. Black dots are from the present work, blue asterisks are taken from Ref. 21, red dots are from Ref. 22, and green diamonds are from Ref. 29. We argue that for $E_{\rm F} > 0$, the G′ band of Ref. 21 is explained by the KA effect, therefore, it follows our trend of the $\rm G'_i$ band. However for $E_{\rm F} < 0$, the G′ band of Ref. 21 is explained by the quantum interference effect in which the $\rm G'_i$ intensity becomes smaller than the $\rm G'_m$ intensity. Thus the total G′ peak position increases when $E_{\rm F}$ increases. The discrepancy with Ref. 21 could not be well-explained because we do not consider the static Kohn anomaly effect that was involved in Ref. 21.

It is important to note that electron-electron interactions might contribute to the Raman resonance window or carrier scattering rate γ[57]. In this calculation, γ is considered to be a function of $E_{\rm L}$ only. By including the electron-electron interaction, γ for the second-order Raman spectra will increase proportionally to $E_{\rm F}$[57]. The second-order Raman intensity will be reduced even at a low doping. Our prediction related to the intensity enhancement of the combination phonon modes (iTA+iTO and $\rm G^*$ bands) might not be observed experimentally due to the electron-electron interactions. Therefore, experimental confirmations are necessary to understand whether or not the electron-electron interaction is significant to suppress the quantum interference effect.

IV. CONCLUSION

In conclusion, we calculated the first- and second-order Raman spectra as a function of $E_{\rm F}$. The opposite effect of the Kohn anomaly that is found experimentally between the first- and the second-order Raman spectra occurs be-

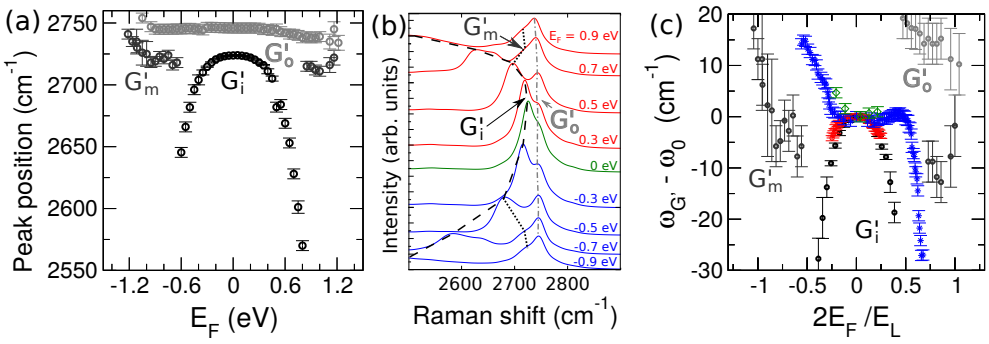

FIG. 11. (Color online) (Color online) (a) Peak positions of G'_i, G'_m, and G'_o bands as a function of E_F. (b) Evolution of the G' band for several values within $[-0.9, 0.9]$ eV. Dashed line, dotted line, and dashed-dotted line are guide for eyes to show the evolution of peak positions of G'_i, G'_m, and G'_o bands, respectively. (c) The G' band peak shift as a function of $2E_F/E_L$. Black dots are this work, blue asterisks are from Ref. 21, red dots are from Ref. 22, and green diamonds are from Ref. 29.

cause the KA effect on the first-order Raman spectra is dominated by the renormalization of phonons by the interband electron-hole excitation, while in the second-order Raman spectra, the intraband electron-hole excitation dominates over the KA effect. We also discussed the quantum interference effect observed in the change of the Raman intensity as a function of E_F. Both the first- and the second-order Raman spectra exhibit an impact of the quantum interference effect, especially when $2|E_F| \approx E_L$. Present calculated results found that not only is the resonance condition important, but also the explicit consideration of the electron-phonon matrix elements are essential to determine the E_F dependence of the Raman intensity. The matrix element effect play an important role in the intensity increase (decrease) of the combination (overtone) phonon modes as a function of E_F.

ACKNOWLEDGMENTS

E.H. is supported by a MEXT scholarship. A.R.T.N. acknowledges the Interdepartmental Doctoral Degree Program for Material Science Leaders at Tohoku University for providing a financial support. R.S. acknowledges MEXT Grants No. 25286005 and No. 225107004. M.S.D. acknowledges NSF-DMR Grant No. 15-07806.

* Electronic Address: hasdeo@flex.phys.tohoku.ac.jp

[1] Y. Zhang, V. W. Brar, F. Wang, C. Girit, Y. Yayon, M. Panlasigui, A. Zettl, and M. F. Crommie, Nat Phys **4**, 627–630 (2008).

[2] F. Wang, Y. Zhang, C. Tian, C. Girit, A. Zettl, M. Crommie, and Y. R. Shen, Science **320**, 206–209 (2008).

[3] M. S. Ukhtary, E. H. Hasdeo, A. R. T. Nugraha, and R. Saito, Applied Physics Express **8**, 055102 (2015).

[4] K. S. Novoselov, A. K. Geim, S. V. Morozov, D. Jiang, Y. Zhang, S. V. Dubonos, I. V. Grigorieva, and A. A. Firsov, Science **306**, 666–669 (2004).

[5] K. S. Novoselov, Z. Jiang, Y. Zhang, S. V. Morozov, H. L. Stormer, U. Zeitler, J. C. Maan, G. S. Boebinger, P. Kim, and A. K. Geim, Science **315**, 1379–1379 (2007).

[6] Y. Zhang, Y.-W. Tan, H. L. Stormer, and P. Kim, Nature **438**, 201–204 (2005).

[7] M. I. Katsnelson, K. S. Novoselov, and A. K. Geim, Nat Phys **2**, 620–625 (2006).

[8] C. W. J. Beenakker, Rev. Mod. Phys. **80**, 1337–1354 (2008).

[9] C. Popovici, O. Oliveira, W. de Paula, and T. Frederico, Phys. Rev. B **85**, 235424 (2012).

[10] K. Sengupta and G. Baskaran, Phys. Rev. B **77**, 045417 (2008).

[11] Z. Jiang, Y. Zhang, H. L. Stormer, and P. Kim, Phys. Rev. Lett. **99**, 106802 (2007).

[12] K. Kechedzhi, E. H. Hwang, and S. Das Sarma, Phys. Rev. B **86**, 165442 (2012).

[13] M. F. Craciun, S. Russo, M. Yamamoto, J. B. Oostinga, A. F. Morpurgo, and S. Tarucha, Nat. Nano **4**, 383 (2009).

[14] Y. Zhang, T. Tang, C. Girit, Z. Hao, M. C. Martin, A. Zettl, M. F. Crommie, Y. R. Shen, and F. Wang, Nature **459**, 820–823 (2009).

[15] V. V. Cheianov, V. Fal'ko, and B. L. Altshuler, Science **315**, 1252–1255 (2007).

[16] F. Xia, T. Mueller, Y. Lin, A. Valdes-Garcia, and P. Avouris, Nat Nano **4**, 839–843 (2009).

[17] R. Saito, K. Sato, P.T. Araujo, D.L. Mafra, and M.S. Dresselhaus, Solid State Communications **175-176**, 18–34 (2013).

[18] W. Kohn, Phys. Rev. Lett. **2**, 393 (1959).

[19] S. Piscanec, M. Lazzeri, F. Mauri, A. C. Ferrari, and J. Robertson, Phys. Rev. Lett. **93**, 185503– (2004).

[20] M. Lazzeri and F. Mauri, Phys. Rev. Lett. **97**, 266407 (2006).

[21] A. Das, S. Pisana, B. Chakraborty, S. Piscanec, S. K. Saha, U. V. Waghmare, K. S. Novoselov, H. R. Krishnamurthy, A. K. Geim, A. C. Ferrari, and A. K. Sood, Nat Nano **3**, 210–215 (2008).

[22] P. T. Araujo, D. L. Mafra, K. Sato, R. Saito, J. Kong, and M. S. Dresselhaus, Phys. Rev. Lett. **109**, 046801 (2012).

[23] C.-F. Chen, C.-H. Park, B. W. Boudouris, J. Horng, B. Geng, C. Girit, A. Zettl, M. F. Crommie, R. A. Segalman, S. G. Louie, and F. Wang, Nature **471**, 617–620 (2011).

[24] J. Liu, Q. Li, Y. Zou, Q. Qian, Y. Jin, G. Li, K. Jiang, and S. Fan, Nano Letters **13**(12), 6170–6175 (2013).

[25] S. Y. Zhou, D. A. Siegel, A. V. Fedorov, and A. Lanzara, Phys. Rev. B **78**, 193404 (2008).

[26] D. Yoon, D. Jeong, H. Lee, R. Saito, Y. Son, H. Lee, and H. Cheong, Carbon **61**, 373 – 378 (2013).

[27] E. H. Hasdeo, A. R. T. Nugraha, M. S. Dresselhaus, and R. Saito, Phys. Rev. B **90**, 245140 (2014).

[28] D. L. Mafra, J. Kong, K. Sato, R. Saito, M. S. Dresselhaus, and P. T. Araujo, Phys. Rev. B **86**, 195434 (Nov 2012).

[29] J. Yan, Y. Zhang, P. Kim, and A. Pinczuk, Phys. Rev. Lett. **98**, 166802 (2007).

[30] K. Sasaki, R. Saito, K. Wakabayashi, and T. Enoki, Journal of the Physical Society of Japan **79**, 044603 (2010).

[31] W. Ren, R. Saito, L. Gao, F. Zheng, Z. Wu, B. Liu, M. Furukawa, J. Zhao, Z. Chen, and H.-M. Cheng, Phys. Rev. B **81**, 035412 (2010).

[32] T. Ando, J. Phys. Soc **75**, 124701 (2006).

[33] A. C. Ferrari, Solid State Communications **143**, 47 – 57 (2007).

[34] C. Thomsen and S. Reich, Phys. Rev. Lett. **85**(24), 5214–5217 (2000).

[35] K. Sasaki, K. Kato, Y. Tokura, S. Suzuki, and T. Sogawa, Phys. Rev. B **86**, 201403 (2012).

[36] J. Jiang, R. Saito, A. Grneis, G. Dresselhaus, and M.S. Dresselhaus, Chemical Physics Letters **392**, 383 – 389 (2004).

[37] K. Sasaki and R. Saito, Prog. Theor. Phys. **176**, 253–278 (2008).

[38] P. Venezuela, M. Lazzeri, and F. Mauri, Phys. Rev. B **84**, 035433 (2011).

[39] R. M. Martin and L. M. Falicov, in *Light Scattering in Solids I: edited by M. Cardona*, pages 79–145, (Springer-Verlag, Berlin, 1983), Vol. 8. Chapter 3, Topics in Applied Physics.

[40] J. Maultzsch, S. Reich, , and C. Thomsen, Phys. Rev. B **70**, 155403 (2004).

[41] V. N Popov, New J. Phys. **6**, 17 (2004).

[42] Ge. G. Samsonidze, R. Saito, N. Kobayashi, A. Grüneis, J. Jiang, A. Jorio, S. G. Chou, G. Dresselhaus, and M. S. Dresselhaus, Appl. Phys. Lett. **85**, 5703 (2004).

[43] O. Dubay and G. Kresse, Phys. Rev. B **67**, 035401 (2003).

[44] R. Saito, M. Furukawa, G. Dresselhaus, and M. S. Dresselhaus, Journal of Physics: Condensed Matter **22**, 334203 (2010).

[45] J. Maultzsch, S. Reich, C. Thomsen, H. Requardt, and P. Ordejon, Phys. Rev. Lett. **92**, 075501 (2004).

[46] M. Mohr, J. Maultzsch, E. Dobardzic, S. Reich, I. Milosevic, M. Damnjanovic, A. Bosak, M. Krisch, and C. Thomsen, Phys. Rev. B **76**, 035439 (2007).

[47] A. Grüneis, J. Serrano, A. Bosak, M. Lazzeri, S. L. Molodtsov, L. Wirtz, C. Attaccalite, M. Krisch, A. Rubio, F. Mauri, and T. Pichler, Phys. Rev. B **80**, 085423 (2009).

[48] A. Grüneis, R. Saito, Ge. G. Samsonidze, T. Kimura, M. A. Pimenta, A. Jorio, A. G. Souza Filho, G. Dresselhaus, and M. S. Dresselhaus, Phys. Rev. B **67**, 165402 (2003).

[49] J. Jiang, R. Saito, K. Sato, J. S. Park, Ge. G. Samsonidze, A. Jorio, G. Dresselhaus, and M. S. Dresselhaus, Phys. Rev. B **75**, 035405 (2007).

[50] K. Sasaki, R. Saito, G. Dresselhaus, M. S. Dresselhaus, H. Farhat, and J. Kong, Phys. Rev. B **78**, 235405 (2008).

[51] K Sasaki, K. Kato, Y Tokura, S Suzuki, and T. Sogawa, Phys. Rev. B **85**, 075437 (2012).

[52] D. L. Mafra, G. Samsonidze, L. M. Malard, D. C. Elias, J. C. Brant, F. Plentz, E. S. Alves, and M. A. Pimenta, Phys. Rev. B **76**, 233407 (2007).

[53] S. Berciaud, X.L. Li, H. Htoon, L. E. Brus, S. K. Doorn, and T. F. Heinz, Nano Letters **13**, 3517–3523 (2013).

[54] R. Rao, R. Podila, R. Tsuchikawa, J. Katoch, D. Tishler, A. M. Rao, and M. Ishigami, ACS Nano **5**, 1594 (2011).

[55] H.-L. Liu, S. Siregar, E. H. Hasdeo, Y. Kumamoto, C.-C. Shen, C.-C. Cheng, L.-J. Li, R. Saito, and S. Kawata, Carbon **81**, 807 – 813 (2015).

[56] M. Bruna, A. K. Ott, M. Ijs, D. Yoon, U. Sassi, and A. C. Ferrari, ACS Nano **8**, 7432–7441 (2014).

[57] D. Basko, S. Piscanec, and A. Ferrari, Phys. Rev. B **80**, 165413 (2009).